Case Studies in Thermal Engineering 56 (2024) 104233

Contents lists available at ScienceDirect

Case Studies in Thermal Engineering

journal homepage: www.elsevier.com/locate/csite

An integrated 2D/3D numerical methodology to predict the thermal field of electric motors

Clara Iacovano [a], Fabio Berni [a,*], Giuseppe Cicalese [b], Stefano Nuzzo [a], Stefano Fontanesi [a]

[a] Department of Engineering "Enzo Ferrari" (DIEF), University of Modena and Reggio Emilia, Modena, Italy
[b] R&D CFD s.r.l., Modena, Italy

A B S T R A C T

The present work aims at providing a predictive numerical methodology for the thermal characterization of electric motors. The methodology relies on a 2D-FE simulation for the estimation of the electromagnetic (iron and joule) losses. The latter are then exploited in a 3D-CFD Conjugate Heat Transfer analysis for the evaluation of the thermal field.

The CFD model includes both the solid components and the fluid domains. The main novelty of the paper is represented by the copper coil modelling. In fact, copper, air, epoxy resin and enamel are synthetized in a single homogeneous body able to reproduce the thermal behaviour without including the single components, to reduce the computational cost.

The methodology is validated against experimental data on a three-phase squirrel-cage induction motor. As for the experimental data (available at three different operating conditions), temperature distributions are measured by thermocouples at the test bench for the validation of the 3D-CFD CHT model. In addition, experimental estimations of the losses are available for the validation of the 2D electromagnetic simulations.

The numerical results in terms of motor performance, electromagnetic losses and thermal field are discussed and are proved to be close to the experimental counterparts, for all the investigated conditions.

1. Introduction

Although electric motors provide high efficiency and power-density, the electric power that is not converted to mechanical one produces a non-negligible amount of heat which can range from hundreds to thousands of Watts according to load, speed and motor type [1,2]. If the heat is not properly removed, it can lead to a dangerous thermal state, able to compromise life and safe operation of the motor. Moreover, the smaller the motor is, the more difficult the heat removal becomes.

The main heat sources are due to phenomena such as Joule effect, eddy currents and hysteresis. According to the specific electric motor, such phenomena can have different weight on the total heat source.

In rotating machines, friction and windage losses need to be accounted in the energy balance as well. Finally, additional losses are generated due to the inhomogeneous distribution of current in the wires [3] and the scattering in the production process.

Generally, the temperature distribution is not uniform, with the highest values located on the wires which, surrounded by insulation materials, have a very low dissipation factor. The maximum achievable temperatures are constrained by the thermal properties of the coil insulator, which identifies the class of insulation of the machine. A significant thermal stress determines the thermal aging of the insulation system, resulting in a decay of electrical insulation properties and, thus, shortening the lifespan of the motor [4]. In an induction device, high thermal stress may lead to bar fault and cage fracture at the joint between the bars of the squirrel cage and the rings [4]. Although Joule losses are negligible in rotors of Permanent Magnets Synchronous Motors (PMSM) operating at relatively low

* Corresponding author.
E-mail address: fabio.berni@unimore.it (F. Berni).

https://doi.org/10.1016/j.csite.2024.104233
Received 20 December 2023; Received in revised form 5 March 2024; Accepted 8 March 2024
Available online 23 March 2024
2214-157X/© 2024 The Authors. Published by Elsevier Ltd. This is an open access article under the CC BY-NC-ND license (http://creativecommons.org/licenses/by-nc-nd/4.0/).

frequencies, the losses in the magnets can be elevated at high frequency and, due to the difficulties in cooling rotating bodies, high temperatures can be reached. The magnetic properties of the magnets change significantly with temperature, thus causing performance deterioration and, in the worst case scenario, the irreversible demagnetization [5].

In this context, to limit the temperature rise and, thus, to increase the peak torque [6,7], thermal investigations are mandatory. Besides experiments, Lumped Parameter Thermal Network (LPTN) [8–10] and 3D-CFD/FEA approaches can be proficiently adopted to study and optimize the cooling system geometry, to predict heat path and temperature field and to test pioneering solutions, reducing time and costs of the design stage. Moreover, critical components of an electric motor, such as rotor windings or rotor magnets, whose investigation is usually complex via experiments, can be more easily analysed. Furthermore, during the start of induction motors, temperatures of stator and rotor windings can reach significantly high values. A transient characterization of the start under several loads is not experimentally straightforward, while it is achievable by means of thermal models [11] in which the multi-physics coupling method accounts for the mutual interaction between electromagnetic phenomena and thermal field [12]. In Ref. [13] P. Ponomarev et al. proposed a comparison between LPTN, FEM and CFD for the thermal modelling of an oil-cooled PMSM. The analytical method provides a quick (even if rough) estimation of the temperature while both FEM and CFD, the latter based on the Conjugate Heat Transfer (CHT) approach, result more suitable tools for the selection of the optimal cooling strategy, but at the expense of higher effort in the model preparation.

Focusing on the design aspects, the cooling system is chosen according to the class of insulation, the operating power and the working environment. Typically, for industrial applications, electric motors are air cooled by natural convection through its surface fins or by forced convection via fans [11,14–19,34]. They are low cost and poor maintenance is required, but their application is limited because of the low power density. The efficiency of fins in the air cooling system of a switched reluctance motor is numerically investigated in Ref. [1] by an unsteady multi-physics study in which the electromagnetic tool provides the heat sources in the heat transfer analysis. Several CFD calculations are employed to optimize the fan design and to reduce noise issues for electric motor air cooling, in which the air motion is accounted for by the Moving Reference Frame approach [14–19].

Higher cooling performance is provided by direct and/or indirect liquid forced convection, which is widely used for high density power motors [20–33]. Generally, the liquid flows through the cooling jacket which surrounds the motor housing. Usually, the adopted coolant is a mixture of water and glycol [20]. In [20–24] several architectures of cooling jacket are analysed by means of CFD, searching the best trade-off between heat transfer capability and pressure drop. In Ref. [23] the authors numerically compare four different cooling technologies such as conventional cooling jacket within the case, circular and rectangular cooling channels within the stator and Direct Winding Heat Exchanger (DWHX), in a PMSM. The study points out that the best cooling performance is provided by the DHWX thanks to the wide heat transfer area and the low thermal resistance resulting from the small distance between heat source and cooling system. The embedded circular and rectangular channels show high heat removal capability but they affect the electro-magnetic performance reducing the global efficiency.

Although the liquid cooling performs better than the air one, it is more expensive as it requires a complex system with radiator and pump. Moreover, the weight increases along with the energy consumption, to run both cooling pump and radiator fan.

Unlike the active windings, the end-windings are surrounded by a significant amount of air, which has extremely low thermal conductivity. The end-windings cooling can be promoted via potting silicone gelatin between them and the motor casing, enhancing the direct heat transfer towards the case and, therefore, to the cooling jacket. This is pointed out in Ref. [25] where a PMSM is experimentally and numerically investigated under several unsteady operating conditions. The 3D model predicts well the extension of stable running time from 84s to 165s under the peak-condition, made possible thanks to the adopted cooling strategy.

An alternative direct cooling solution employs oil jets on the end-windings [4,13,26–33]. In Ref. [26], besides a submerged jet, also an oil spray on hairpin end-windings is investigated, introducing Discrete Phase Model, droplet breakup and coalescence model. Under the liquid jet regime, the Volume of Fluid formulation is commonly used to model the oil-air interaction inside the motor [28,32]. Oil is used for both lubrication and cooling in an integrated electrical motor and gearbox architecture in Ref. [33], in which LPTN model, CFD analysis and laboratory tests confirm the validity of the calculation methods. However, this cooling strategy compromises the cooling uniformity and affects noticeably the cost.

Pulsating heat pipe [34–36], refrigerant [37], phase change material [24], strip spoiler [38] and nanofluids [22] are widely investigated in literature as well.

Moreover, to limit the temperature rise, the design of solid components is deeply examined in Ref. [39]. In order to minimize eddy current and hysteresis losses, both stator and rotor blocks are obtained via sheet lamination process.

Innovative solutions, such as hairpin technology [40–44] to minimize the electric resistance of the windings and High-Temperature Superconductor [45] to reduce the iron losses, are widely studied.

In the present work, a multi-physics analysis of a three-phase induction motor is carried out. The power losses resulting from 2D electromagnetic simulations are applied as source term in the energy equation of the 3D-CFD model. Multi-phase steady-state CFD CHT simulations are performed under three operating conditions. The main goal of the present paper is the proposal of a robust, experimentally validated methodology, able to predict properly performance, electromagnetic losses and thermal field of electric motors. The methodology is meant to be adopted at the design stage, to evaluate the thermal behaviour and its strength derives from the adoption of very detailed models both for 2D and 3D simulations. In particular, for the latter, all the solid components are included as well as the fluid domains, i.e. air gap and cooling circuit. In this regard, particular care is dedicated to both the representation of the contacts between the solids (by means of a proper set of resistances) and the simulation of the internal turbulent flows. The main novelty of the present paper is represented by a dedicated approach to model the stator slot components (namely enamelled copper wires, epoxy resin, air and insulating nomex), in order to mimic the resulting thermal behaviour without including each single element. The adoption of a homogeneous solid instead of the detailed geometry allows to strongly reduce the computational cost.

In the next section, the experimental apparatus and the data of the aforementioned operating points are shown. Then, the setup of both the electromagnetic and fluid dynamic models is introduced. In particular, an in-depth analysis of the thermal coil modelling inside the stator slots is carried out, in which an equivalent homogeneous and orthotropic material mimicking the real coil is proposed. Finally, both 2D-electromagnetic and 3D-CFD results are discussed and conclusions are drawn.

2. Experimental apparatus

The analysed three-phase induction motor is produced by Lucchi R. s.r.l. and it is a 4 pole machine, made of squirrel-cage with 40 short-circuited rotor bars and stator with 48 slots. The stator winding is a double-layer one, with 4 slots-per-pole-per-phase and with a short pitch by 3 slots. The impregnation process is obtained by immersion of the stator in a resin tank which leaves a significant amount of air inside the quarries and in the volume inside the end windings. The air percentage is estimated to be 35% of the volume cave.

Both stator and rotor blocks are made of M400-50 steal lamination stacks with 0.5 mm thick sheets. Rotor cooling vanes, also named wafters, are attached to the rotor ends, acting as a fan and improving the convective heat transfer with the air.

A spiral-shape water jacket surrounds the entire motor housing and it is the main cooling system. It is fed by a water-ethylene glycol mixture (80%–20% by volume).

For the validation of both the losses provided by the 2D electromagnetic simulations and the temperatures calculated by the 3D-CFD CHT model, experimental measurements are performed.

It is useful to point out that, in induction motors, the iron losses in the rotor block are proportional to both stator current frequency f and slip s. Since s is typically very small, the rotor iron losses are not considered because of their negligible contribution. For this reason, they will be neglected in the following.

Firstly, no-load operations are experimentally tested to evaluate friction and windage losses. The sum of the two, for a given revving speed, is determined as the difference between electric power and mechanical one at low current.

Afterward, a thermal characterization of the motor is performed under three load conditions, increasing the value of the stator current. In these tests, temperatures of the components and losses are measured, the latter being evaluated, once again, as difference between electric power and mechanical one. Such losses are the sum of stator iron losses, stator windings Joule losses, rotor Joule losses, friction losses and windage losses. Interestingly, friction and windage losses are considered invariant with and without load, on equal revving speed and current frequency. Therefore, their sum under load is supposed to be known thanks to the no-load tests. As a result, tests under load can provide an estimation of the sum of Joule losses (in stator and rotor) and stator iron losses.

Temperatures of copper, stator and coolant at the inlet/outlet sections of the cooling jacket are measured by means of 11 thermocouples with an error band of $\pm$ (0.7 °C + 0.15%T). Nine of them are placed on wires and stator block, as shown in Fig. 1. A significant difference of temperature is measured between the upper and lower portions of each end-winding (i.e. between T5 and T7 and between T4 and T6). According to the uncertainty and randomness of the end-winding composition, local measurements of temperature could be strongly affected by the inhomogeneity of the copper coil components. This detail cannot be predicted by a 3D model, which has an axis-symmetric setup. For this reason, in the following analysis, the average values between T5 and T7 and between T4 and T6 are used as reference data for right side and left side of the end windings, respectively.

Table 1 shows the main experimental data for the three investigated conditions. Moving from Operating Point (O.P.) A to O.P. B, the magnitude of the stator current decreases, leaving the current frequency (and, consequently, the motor speed) unchanged. Conversely, both electric and mechanical powers decrease.

At O.P. C, the current frequency decreases along with the motor speed. A slight increase in the current magnitude is set, resulting in

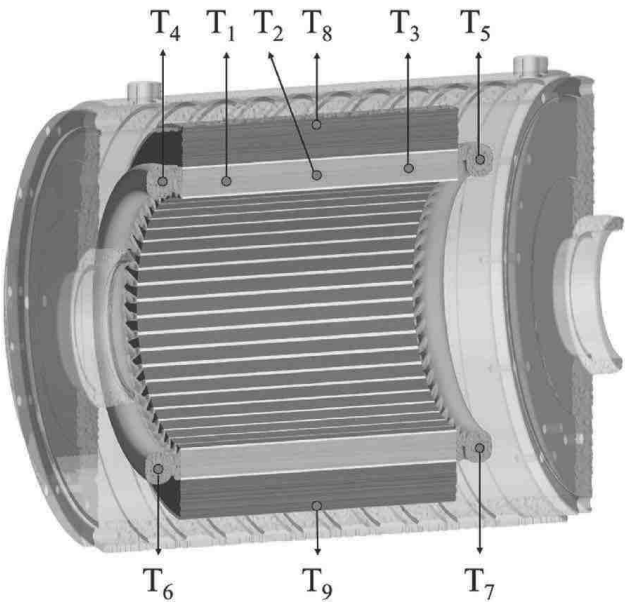

Fig. 1. Position of the thermocouples.

Table 1
Main experimental data.

	Operating Point A	Operating Point B	Operating Point C
	40 kW @1770 rpm	32 kW @1780 rpm	37 kW @1450 rpm
Frequency [Hz]	60.15	60.10	49.76
Torque [Nm]	218.0	174.0	245.1
Mechanical Power [kW]	40.43	32.44	37.24
Electric Power [kW]	44.43	35.32	42.00
Total Losses [kW] (Electric P. - Mechanical P.)	4.00	2.88	4.76
Friction Losses [kW]	0.327	0.327	0.190
Line Current [A]	538.2	421.8	607.7
Phase Current [A]	310.7	243.5	350.9
Slip [−]	0.02	0.01	0.03
T Inlet Coolant [°C]	40.0	40.0	40.0
ΔT (Inlet/Outlet) Coolant [°C]	6.3	4.5	7.4
Coolant Volumetric Flow Rate [L/min]	10.0	10.0	10.0
Heat Removed by Cooling Jacket [kW]	4.08	2.91	4.78

an increase of mechanical torque and total losses.

The motor dissipates 4, 2.88 and 4.76 kW respectively, with an efficiency equal to nearly 90%.

A thermal balance on the cooling mixture is computed as in Eq. (1).

$$\dot{Q} = \rho \dot{V} c_p (T_{outlet} - T_{inlet}) \tag{1}$$

ρ is the density, $\dot{V}$ the volumetric flow rate and c_p the specific heat of the coolant mixture.

The cooling jacket dissipates 4.08, 2.91 and 4.78 kW. Such values well agree with the total losses reported above (equal to the difference between electric and mechanical powers). The minimal differences are related to the measure uncertainties of the experiments.

3. 2D-FE electromagnetic model

As discussed above, the main objective of the electromagnetic model is to estimate the losses. A finite element (FE) model of the considered induction motor is developed using Simcenter MagNet, licensed by Siemens DISW. A 2D FE analysis is deemed to be the best trade-off between accuracy and computational burden for the considered case study. Regarding the stator winding, the active sides of the modelled coils are properly connected each other and to any other circuital element eventually required. In particular, there are 16 coils per phase with 4 parallel paths, while the 3D end effects are taken into account by including in the circuit some appropriate resistors [46], which are calculated considering the experimentally measured phase resistances and the distribution of the active conductors. Regarding the rotor winding, each aluminium bar is modelled as a solid conductor to take into account the phenomena related to the uneven distribution of the current induced within them, whereas the 3D resistances are neglected considering the

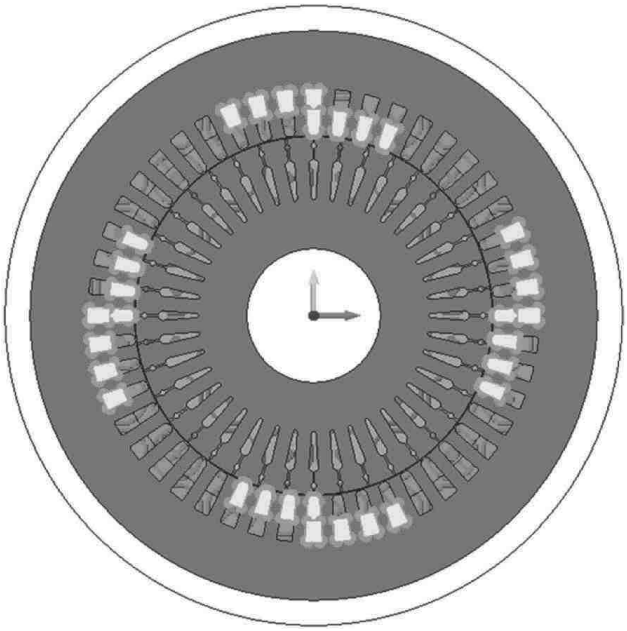

Fig. 2. 2D FE model of the considered induction motor.

relatively high cross section of the short-circuiting rings (which is 16 mm thick). The bars are all connected in parallel and then short-circuited by circuital connection featuring null resistances. A 2D cross section of the developed FE model is shown in Fig. 2, where one of the 3 stator phases is highlighted to comprehensively show the features of the winding layout. In Fig. 2, an external airbox can be also observed, which is introduced to reduce the computational burden. Concerning the mesh, particular attention is given to the parts modelled as "solid", i.e. the rotor bars. The adopted mesh is reported in Fig. 3, with an in-zoom on the rotor bars.

The investigated operating conditions are O.P. A, O.P. B and O.P. C of Table 1. Transient with motion simulations are run, where the moving components are all the rotating parts, whose speed is set considering frequency and slip. Since the rotor bar currents are induced, 4 rotor electric cycles are simulated to reach a steady-state operation. The results of the simulations are discussed in the following sections.

4. 3D-CFD CHT model

In the present paragraph, the 3D-CFD CHT model of the electric motor is presented. The attention is focused on the copper coil modeling at first, which represents the main novelty of the work. Then, the rest of the electric motor 3D-CFD CHT model is described.

4.1. Copper coil model

One of the critical aspects in thermal studies of electric machines is the copper coil modelling. The latter has a heterogeneous structure with insulated electrical conductors surrounded by a mixture of air and resin [23,47].

A schematic example of a stator slot is shown in Fig. 4. The copper coil is composed by a number of enamelled wires, immersed in epoxy resin and air. Insulating nomex surrounds the slot walls. Ideally, the total impregnation of the slot (by means of a vacuum operation) guarantees the total lack of air, leaving space for epoxy and enhancing the thermal conductivity. However, in the currently investigated motor, the impregnation process is made by immerging the stator in a resin tank, thus a large amount of air inside the quarries and into the end windings remains. According to the adopted assembly process applied to the motor, the presence of air is accounted for in the development of the coil model.

From a computational point of view, discretizing each wire of the copper coil is very expensive. The situation worsens moving to the end windings where uncertainties in the geometry and in the composition arise.

In this work, the heterogeneous copper coil body is replaced with a homogeneous material, maintaining similar thermal behaviour thanks to the calculation of equivalent properties.

Starting with the modelling of the nomex insulation, one contact resistance between stator and copper coil and one between the airgap and the copper coil (mimicking the wedge) are set and computed as in Eq. (2).

$$R_c = \frac{s}{\lambda} \tag{2}$$

s is the thickness of nomex and λ is its thermal conductivity.

Moving to the modelling of windings, epoxy, enamel and air, two approaches are considered to obtain equivalent properties (namely density, specific heat and thermal conductivity):

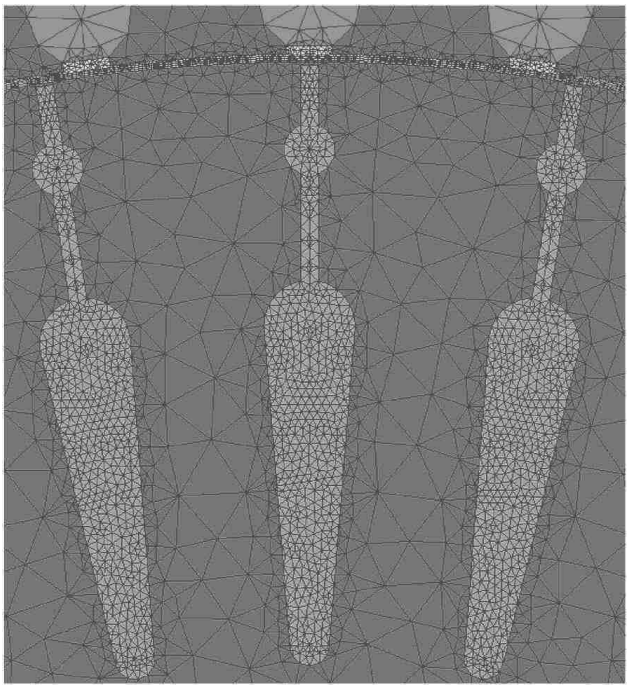

Fig. 3. Mesh in the rotor bars.

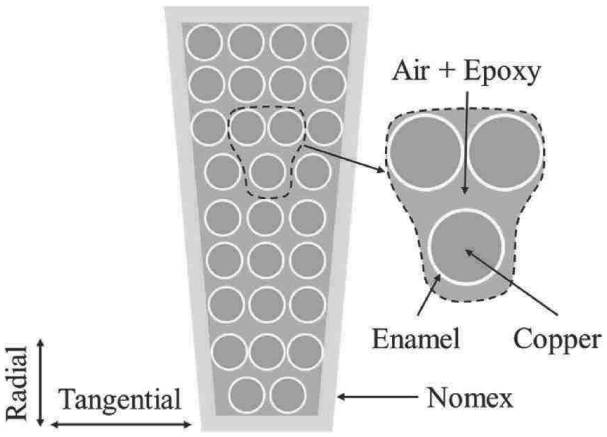

Fig. 4. Illustrative section of a stator cave filled with copper and insulator; radial and tangential directions are indicated.

- *Rule of Mixture (ROM) approach*

The generic material property K is described by a volume-weighted average of the properties of each component following Eqs. (3) and (4), where F_x is the volume fraction of the *x-th* component and K_x its relative property.

$$F_x = \frac{V_x}{V_{air} + V_{epoxy} + V_{enamel} + V_{copper}} \tag{3}$$

$$K = K_{air}F_{air} + K_{epoxy}F_{epoxy} + K_{enamel}F_{enamel} + K_{copper}F_{copper} \tag{4}$$

- *Halpin & Tsai (H-T) approach*

The Halpin & Tsai model is an empirical model used to evaluate the properties of two-phase composite materials made by uniformly distributed and randomly oriented fibers within a matrix. Thanks to the similarity between composite material and coil arrangement in stator caves, H-T formulation is tested in the present work to model their properties. The fiber is the copper wire while the matrix is the mixture of epoxy, air and enamel. The volume fraction of copper F_{copper} is computed by Eq. (3). As for the matrix, the volume fraction of each component ($F_{air}, F_{enamel}, F_{epoxy}$) and the transport property (K_{matrix}) are computed by means of Eqs. (3) and (4) (where only the matrix components are considered in this case). The generic transport property K of the whole copper coil is computed following Eqs. (5) and (6), where ξ is fixed to 1 because of the circular section of the wires.

$$K = K_{matrix} \bullet \frac{1 + \xi\eta F_{copper}}{1 - \eta F_{copper}} \tag{5}$$

$$\eta = \frac{\frac{K_{copper}}{K_{matrix}} - 1}{\frac{K_{copper}}{K_{matrix}} + \xi} \tag{6}$$

With both the approaches, the generic (thermal or mechanical) property K needs to be adjusted, accounting for the thickness of the nomex which is not modelled. In fact, neglecting the thickness of the nomex means overestimating the volume fractions of epoxy, air, enamel and copper.

In radial and tangential directions, the corrective factors (to be adopted as multiplying factors of the equivalent properties) are respectively defined in Eqs. (7) and (8).

$$f_{radial} = \frac{h_{slot}}{\left(h_{slot} - s_{nomex-stator} - s_{nomex-airgap}\right)} \tag{7}$$

$$f_{tangential} = \frac{l_{slot}}{\left(l_{slot} - 2 \bullet s_{nomex-stator}\right)} \tag{8}$$

h_{slot} and l_{slot} are height and width of the cave respectively, $s_{nomex-stator}$ is the thickness of the insulation nomex between stator and copper coil and $s_{nomex-airgap}$ is the thickness of the insulation nomex between airgap and copper coil.

In order to identify the best approach for the coil modelling, without the uncertainties of the motor operation, a simplified numerical test is performed in which copper wires and matrix are physically distinguished. This test is used for validation purpose of the methodology.

The 3D-sketch of the test case is shown in Fig. 5, in which copper and matrix are orange and grey coloured respectively. It is a long parallelepiped characterized by a rectangular cross-section. The domain extension is 4x5x500 mm and the diameter of the wire is 1

mm. The coil composition is described in Table 2.

Density, specific heat and thermal conductivity of the matrix are computed using the ROM approach, while the wire properties are the copper ones. Fig. 5 shows the boundary conditions imposed on the walls as well. At the interface between matrix and wires, a thermal contact resistance equal to $1.34 \bullet 10^{-4}$ m^2K/W models the enamel. Therefore, the matrix is made of air and resin. Both regions are discretized by a polyhedral mesh, extruded for 500 mm with 50 layers. The base size is 1 mm which decreases up to 0.05 mm. The total number of cells is 82700.

In order to account for the lack of enamel in the model, the corrective factor reported in Eq. (9) is used in the radial and tangential directions.

$$f_{trasversal} = \frac{Matrix\ Area}{Matrix\ Area - 5 * (Enamel\ Area)} \tag{9}$$

Simultaneously, a 3D-CFD model is created with the same dimensions, coil composition, mesh, boundary of the former, but with matrix and wires merged into a unique homogeneous component. The thermal conductivity is computed with both ROM and H-T approaches. In particular, two setups are tested: in the first one the thermal conductivity is computed by means of the ROM approach and applied along all the directions. In the second setup, the thermal conductivity is computed by means of the H-T formulation along the radial and tangential directions and by the ROM approach along the longitudinal (axial) one, defining an orthotropic body. Density and specific heat are only computed with the ROM approach.

Steady-state simulations are carried out via a commercial 3D-CFD software, namely STAR-CCM+, licensed by Siemens DISW and they are focused on the temperature field. The latter is shown in Fig. 6a), 6b) and 6c), on a transversal plane, for the three presented approaches. As for the reference case, according to the boundary conditions, a temperature gradient is predicted along the radial direction. The ROM approach does not provide a proper temperature gradient, suggesting an overestimation of thermal conductivity. In fact, the latter is closer to the value of copper than to the matrix one. Moreover, the mean temperature value is lower than the one computed by the reference case. Conversely, the hybrid H-T/ROM approach allows a proper prediction of both temperature distribution and mean value, thanks to the equivalent thermal conductivity in the radial and tangential directions closer to the matrix property than to the copper one. The main difference between the reference case and the hybrid H-T/ROM formulation appears at the wire location where the high thermal conductivity of the copper induces a local isothermal behaviour. This aspect is not predicted by the homogeneous body, which cannot account for local effects induced by the wires as they are not present.

Nonetheless, the hybrid H-T/ROM formulation appears to be more suitable for the active windings modelling than the pure ROM one.

As for the end-windings, a simplified homogeneous toroidal solid domain with equivalent properties and a volume equal to the sum of the volumes of the single components (namely wire, enamel, air and epoxy resin) is defined, similarly to the active windings. However, in this case, the actual random spatial distribution of fibres and the lack of knowledge about a specific composition make the H-T approach inappropriate. Therefore, the ROM formulation is preferred along all the directions, for all the properties.

4.2. Electric motor model

The analysis is performed still by STAR-CCM+. Multi-phase steady-state simulations are carried out, including both solid and fluid components which exchange energy through interfaces.

The motor geometry is simplified neglecting screws, washers, external three-phase wirings and magnetic pick up sensor. Conversely, shaft, bearings, rotor, stator, wires, end windings and case are included.

4.2.1. Solid components

To compute the temperature field in solid bodies, only the energy equation is solved and, according to the steady-state condition, the thermal conductivity λ defines the thermal behaviour. Table 3 shows the main properties of the solid bodies.

To account for the insulating material in the rotor and stator rolled stacks, the thermal conductivity in the axial direction is reduced. Heat sources are assigned to rotor cage, stator block, bearings and wires to account for Joule, hysteresis, eddy current and friction

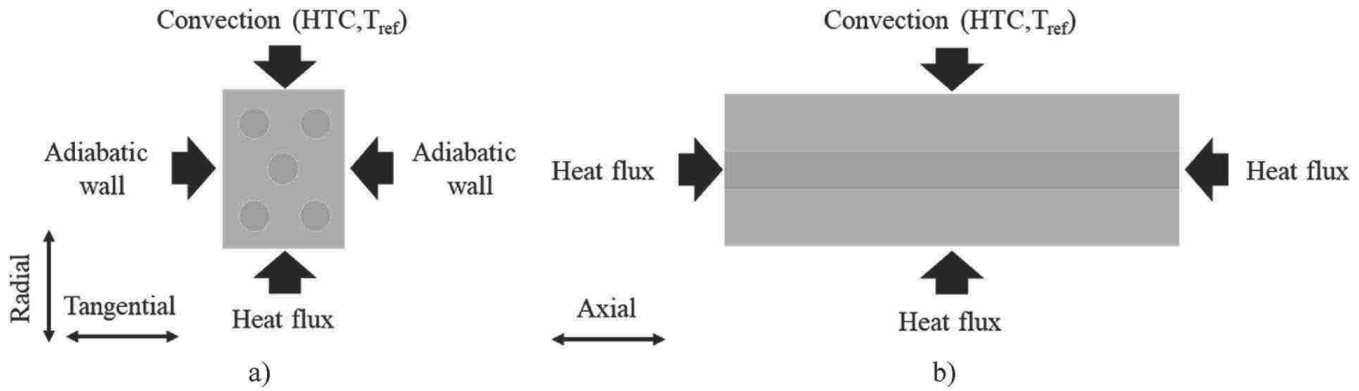

Fig. 5. Sketch and boundary conditions of the test case; a) shows a transversal section while b) a longitudinal one; radial, tangential and axial directions are indicated.

Table 2
Coil composition.

Coil materials	
[% volume fraction]	
Copper	19.5%
Epoxy resin	40.5%
Enamel	5.0%
Air	35.0%

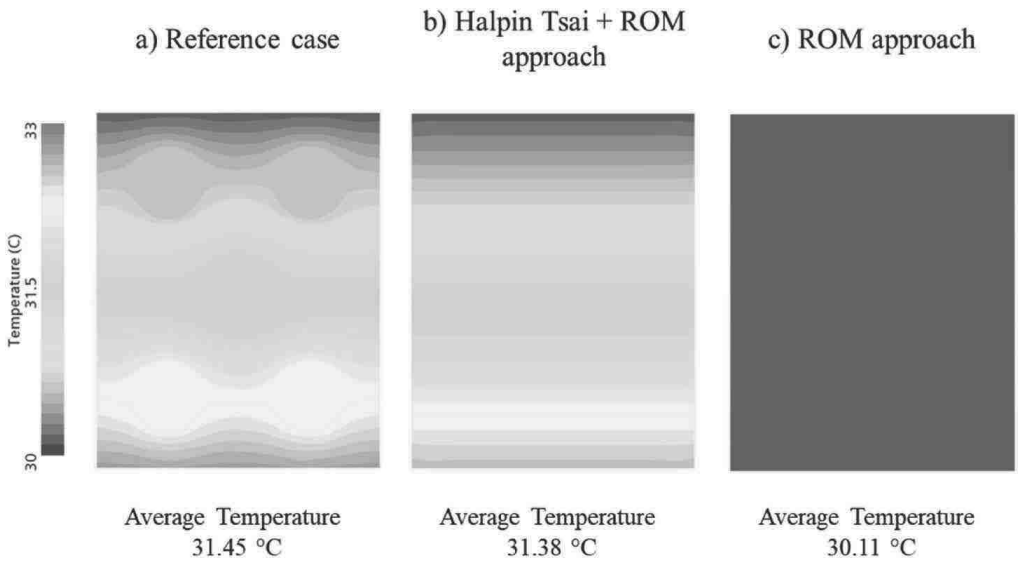

Fig. 6. –Thermal field and average temperature on a transversal section for reference case (a), H-T/ROM approach (b) and ROM approach (c); results are shown for a single central section as a similar temperature behaviour can be noticed regardless the axial position.

Table 3
Material properties of the solid components.

	Shaft	Case	Bearings		Rotor cage	Stator Block		Rotor Block	
			Rings	Body		Axial	Radial	Axial	Radial
Material	Steel 42CrMo4	Al	Steel AISI 440C		Al	Steel M400-50		Steel M400-50	
Density [Kg/m^3]	7800	2790	7700		2790	7650		7650	
Specific Heat [J/KgK]	460	833	480		833	460		460	
Thermal Conductivity [W/mK]	45	160	25	3.42	160	6	28	6	28

losses. All the losses are calculated via the 2D-FE electromagnetic simulations, apart from the friction ones due to the bearings. Friction losses are the only contribution inherited from the experiments and applied to the 3D-CFD model. As previously explained, experiments are able to provide the sum of the losses from friction and windage. Such sum is directly applied to the 3D model as friction losses, i.e. windage losses are assumed to be negligible. This hypothesis will be verified in the results section analysing the outcomes of the CFD model. Moreover, consistently with the electromagnetic model setup in which the electric resistance of the short circuit rings is neglected, the heat source in the rotor cage is assigned only on the rotor bars. All the heat sources are uniformly assigned in the volume of the respective bodies, except for the stator block, in which a volumetric distribution of heat source based on the radius is applied. In this regard, Fig. 7a) shows the volumetric heat source function applied to the stator region at each O.P. and an example of its 3D distribution (the one referred to O.P A) is shown in Fig. 7b). A constant value is imposed along the stator teeth and then a decreasing law is defined up to the maximum radius. For each O.P., the integral of the volumetric heat source function on the stator volume returns the total heat produced by the stator itself, which is provided by the 2D model similarly to all the other electromagnetic losses.

The values of the heat sources applied on each solid component and for each operating point are summarized in the result section dedicated to the 2D-FE simulations.

As discussed in the previous section, the copper coil is modelled as a homogeneous single body, synthetizing properties of wire, enamel, air and epoxy resin. Equivalent density and specific heat are calculated via the ROM approach. The thermal conductivity of the equivalent material is computed by means of the ROM approach in the axial direction and via the H-T method in the radial and tangential directions, while the end windings are exclusively described by the ROM approach. As for the nomex, its presence between stator and cooper coil is considered by a thermal contact resistance. In order to account for the nomex volume, the radial and tangential

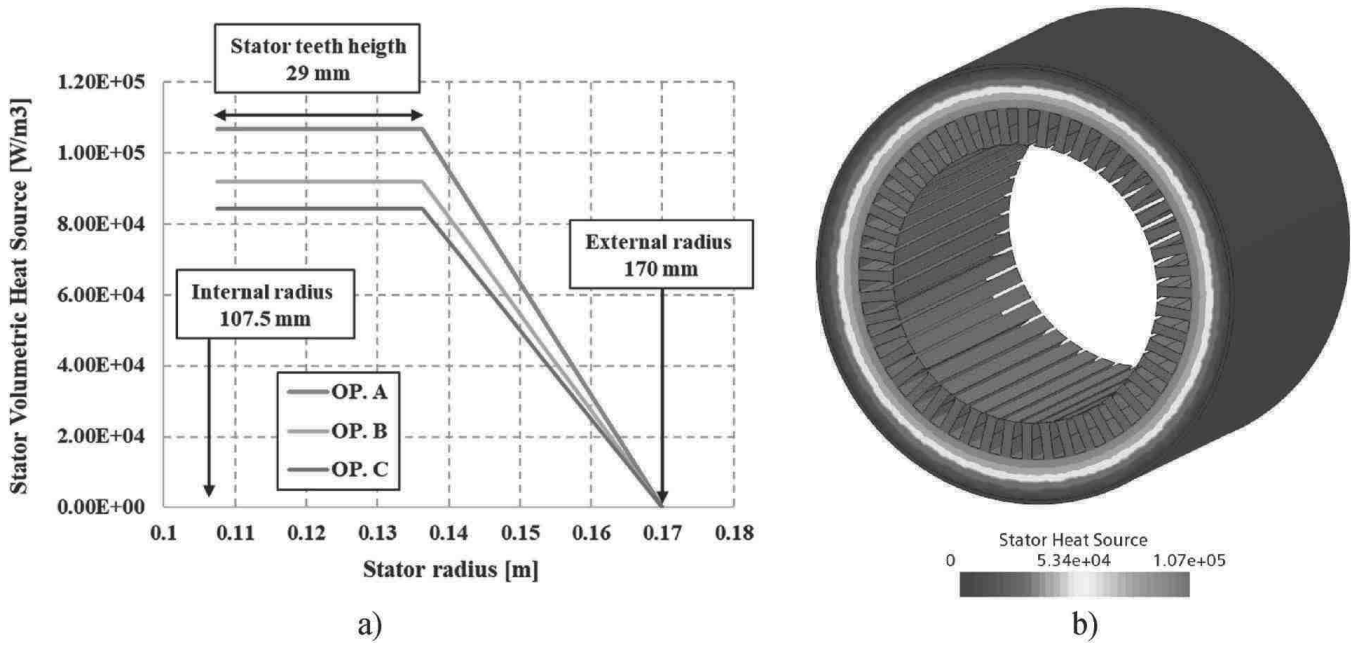

Fig. 7. The stator volumetric heat source as a function of the radius is reported in a), for each operating condition; the 3D distribution of the stator volumetric heat source of O.P. A is shown in b), which corresponds to the red line in a); values in b) are expressed in W/m^3. (For interpretation of the references to colour in this figure legend, the reader is referred to the Web version of this article.)

corrective factors defined in Eqs. (7) and (8) are applied. Table 4 shows the coil composition as volume percentage and the properties of each coil component. Table 5 shows the equivalent properties for the copper coil model.

The total mass of copper in the motor is 19.5÷20 kg and the fraction in the active windings is known thanks to the copper properties and the coil geometry (number and diameter of the wires, volume of each slot and slot length are known). Consequently, mass and volume of copper in the end windings are known as well. According to this, the Joule losses are distributed proportionally to the copper volumes, thus 52% is assigned to the active windings while the remaining 48% is left to the end windings.

Due to the insulator, the coil has a small heat dissipation factor and the peak temperature is placed in the middle of the stator slot. For this reason, the coil is divided into two sub-regions: a core region, equivalent to the total volume of the copper in the cave, and a sheath region, defined by the remaining volume of enamel, epoxy and air. The volumetric heat source is assigned only to the core region. About the thermal properties, instead, core and sheath regions are characterized by the same values (the ones of Table 5).

Moreover, according to the double-layer layout of the windings, for each cave both core and sheath regions are split into two sub-coils by means of a phase separator. The latter is modelled as a contact resistance whose value is shown in Table 6. Fig. 8 clarifies the copper coil structure and the discussed sub-geometries.

All the contact thermal resistances used to save the computational cost are summarized in Table 6. The initial temperature of all the solid components is fixed to 100 °C.

4.2.2. Fluid domains

As for the fluids, both the air in the motor case and the refrigerant in the cooling jacket are simulated. A fluid domain is more computationally expensive than a solid one, because mass, momentum and energy equations need to be solved. In order to properly simulate the rotation of the components without including mesh motion, the air domain is divided in two sub-domains, “rotating” region and “static” one. As for the first, it is identified near the rotating walls such as shaft, bearings and rotor. In this region, the Moving Reference Frame method is applied. As for the latter, it is represented by the remaining portion of the air domain and the governing equations are solved with respect to the stationary reference frame. For the sake of clarity, Fig. 9 shows the sub-domains of air.

Turbulence is modelled by the Realizable k-ε two-layer model. As for the near-wall treatment, an all-y$^+$ approach is preferred, as able to properly compute wall shear stress and wall heat flux regardless the y$^+$ value.

As for the air, Sutherland law is used to evaluate the dynamic viscosity while its specific heat is described by a polynomial function

Table 4
Coil composition and properties of the coil components.

	Copper	Enamel	Epoxy	Air
Density [Kg/m^3]	8940	1150	1150	1.225
Specific Heat [J/KgK]	385	1000	1000	1005
Thermal conductivity [W/mK]	401	0.35	0.2	0.026
Composition [%]	49.9	9.8	5.3	35.0

Table 5
Copper coil thermal properties.

	Coil properties					
	End Windings			Active Windings		
	ROM approach			H. & T. + ROM approaches		
	Axial	Radial	Tangential	Axial	Radial	Tangential
Density [Kg/m^3]	4636.9			4636.9		
Specific Heat [J/KgK]	694.7			694.7		
Thermal conductivity [W/mK]	200.2			200.2	0.33	0.34

Table 6
Contact thermal resistances.

Interface	Contact Resistence [m^{2}K/W]
AirGap - Coil (Nomex)	2.5E-03
Air - EndWinding (Epoxy)	5.0E-03
Stator - Coil (Nomex)	2.2E-03
Phase separator	1.8E-03
Solid - Solid	1.0E-04

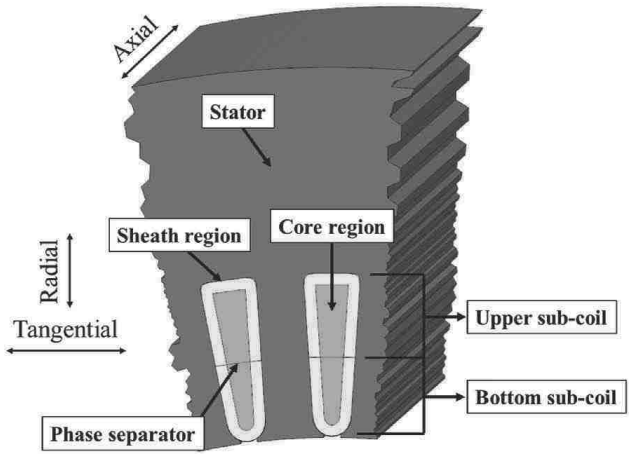

Fig. 8. Slice of stator and copper coil.

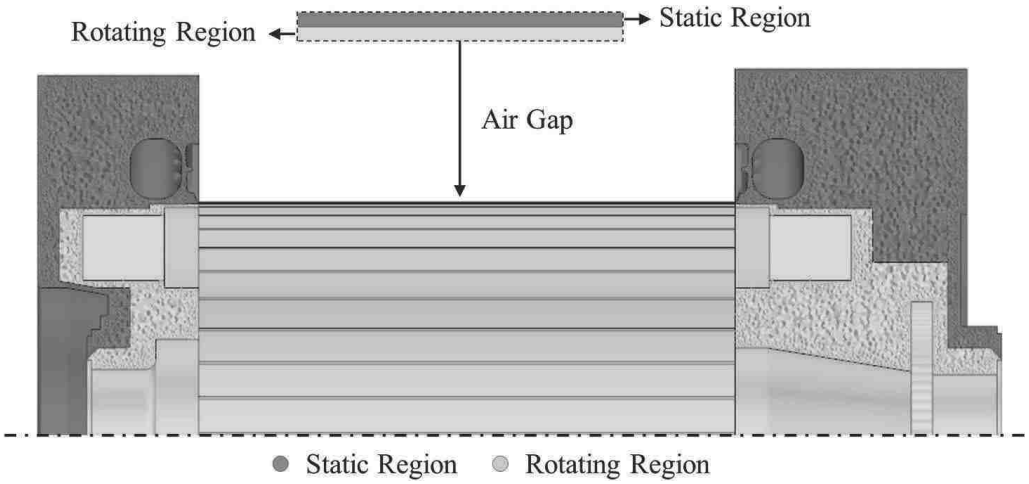

Fig. 9. Static and rotating sub-domains of air.

of the temperature. The ideal gas equation of state is employed to compute the density. The refrigerant fluid is a mixture 80%–20% by volume of water and glycol, respectively.

The density of the refrigerant fluid is computed as volume-weighted average of each component. Specific heat c_p and thermal conductivity λ are computed as mass-weighted averages of the properties of pure water and glycol. The viscosity μ is selected from the Coolprop database, available online, for the adopted composition of the mixture.

As for the boundary conditions of the fluid domain, the volumetric flow rate at the inlet section is set equal to 10L/min and the ambient pressure is set at the outlet section. Table 7 summarizes the main properties of the air and refrigerant domains, as well as the adopted initial conditions. According to the small range of variability of the coolant temperature, density, viscosity, thermal conductivity and specific heat are set as constant.

4.2.3. Computational grid

As for the mesh, Fig. 10a) and 10b) show the computational grid of the motor components. Focusing on case, bearings, shaft and end-windings, a polyhedral mesh with characteristic size equal to 6 mm is implemented. Stator, active windings, rotor blocks and rotor bars are discretized by a polyhedral mesh obtained via extrusion along the axial direction. According to this, the mesh has high cell quality with relatively low number of cells. The characteristic size varies from 0.1 mm up to 4 mm. Static and rotating fluid sub-domains of air are characterized by a polyhedral mesh with characteristic cell size ranging from 0.1 mm to 4 mm; the growth rate is slow in order to ensure small cells in most of the domain. Only in the fluid sub-domains a prismatic near-wall mesh is adopted, with a single layer 0.5 mm thickened. This simple strategy is possible thanks to the adopted all-y + wall treatment which is able to properly simulate the wall quantities even in presence of high y^+ values. The air gap thickness is 0.5 mm and it is discretized by a polyhedral mesh obtained by extrusion in the axial direction. Because of the dimension, the cell size in the air gap varies from 0.01 mm up to 0.1 mm. For the same reason, a dedicated approach is reserved to the near-wall region. Three wall layers are used on both stator and rotor sides, with a total thickness of 0.15 mm for each of them. Moving to the cooling channel, outlet and inlet areas are discretized via a polyhedral mesh with a characteristic size of 2 mm. The main spiral path of the coolant is obtained extruding the polyhedral mesh at the inlet up to the outlet to guarantee a flow-aligned grid. As for the near-wall mesh, 12 layers with a growth factor equal to 1.2 and a total thickness of 1 mm are adopted. The first layer is characterized by very low y^+ values, so that the near-wall cell centroids fall into the low-Reynolds formulation of the all-y^+ wall treatment. The latter allows the integration of momentum and energy equations up to the wall, leading to a more accurate resolution of velocity and temperature profiles in the boundary layer.

Finally, the total number of computational cells necessary to discretize the entire motor is about 20 M. As shown in Appendix A, the adopted overall grid is fine enough to ensure grid-independent results.

5. Results

5.1. 2D-FE electromagnetic results

The results of the electromagnetic analysis for the investigated operating conditions, namely O.P. A, B and C, are proposed in the following. Compared to the experimental measurements reported in Table 1, the performance of the motor in terms of torque is matched for all the operations with an error of ±3% (the calculated torques are 216 Nm, 170 Nm and 250 Nm for the O.Ps. A, B and C, respectively), which is a non-trivial achievement considering the complexities of the involved phenomena. The calculated losses are shown in Table 8. As for the rotor cage, values are not reported as simulations confirm that they can be neglected (they correspond, for each condition, roughly to the 1% of the total amount of losses). For each investigated operation, adding the bearing (friction) losses inherited by the experiments and previously reported in Table 1 to the values of Table 8, it is possible to obtain the total losses which result to be close to the experimental target still reported in Table 1. In particular, the total amount of losses is properly predicted with an error of ±3% (coherently with the estimation of the performance). For the sake of completeness, the time average total loss distribution for O.P. A is provided in Fig. 11. It can be observed that the losses are mainly localized in the rotor bars (while in the rotor core are minimal). As for the stator, the major part of the losses is related to the windings, but a non-negligible contribution can be found in the teeth as well.

5.2. 3D-CFD CHT results

Moving to the thermal behaviour of the motor, a comparison between CFD and experiments is proposed in the present paragraph both in terms of local temperatures and heat rejected to the coolant circuit. For this purpose, consistently with the experimental thermocouples position shown in Figs. 1 and 9 temperature probes are set in the 3D model. Four of them are located in the end winding regions (T_4, T_5, T_6, T_7), three in the active copper coil (T_1, T_2, T_3) and two at the interface between stator and case (T_8, T_9).

Table 7
Properties and initial conditions of air and coolant.

	Air	Coolant
Density [Kg/m^3]	Ideal Gas	1014.1
Dynamic viscosity [Pa*s]	Sutherland's law	0.00101
Specific heat (J/KgK)	Polynomial (T)	3819.6
Thermal conducibility (W/mK)	0.0241	0.547
Initial Temperature (°C)	80	30
Initial Velocity (m/s)	18	1.5

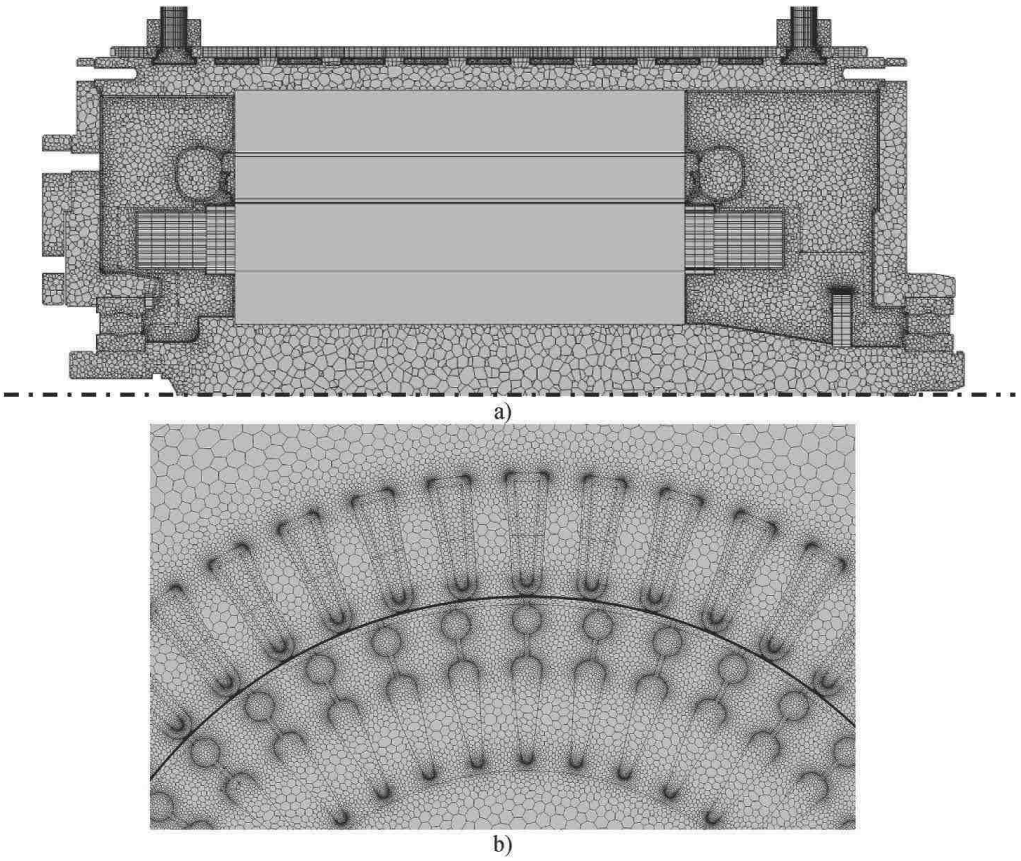

Fig. 10. Numerical grids for case, bearings, shaft, end-windings, air domain and cooling circuit are reported in a), while grids for stator block, active windings, squirrel cage rotor and rotor block are shown in b).

Table 8
Heat sources for the thermal model at the three operating conditions.

	Heat Source [W]		
	O.P. A	O.P. B	O.P. C
Active Stator + End Windings	1254	672	1885
Rotor cage	1705	1233	2251
Stator Core	662	570	522

The first 3D-CFD simulation is carried out at O.P. A to both calibrate and validate the model (specifically, the calibration refers to the adopted contact thermal resistances). The introduction of a proper total heat content is confirmed by the alignment between simulation and experiments in terms of temperature variation of the coolant between inlet and outlet, as visible in Table 9. Thanks to the CFD model, it is possible to point out interesting aspects. For example, the global thermal power introduced in the domain is dissipated by cooling jacket and convection with the environment. However, almost the whole thermal power is rejected to the coolant circuit, specifically the 99.6%. Only the remaining 0.4% is released to the environment. Moreover, the windage loss computed by the CFD is about 10 W, i.e. roughly 3% of the total friction losses experimentally estimated (327 W). This endorses the hypothesis of considering the windage losses as negligible.

Fig. 12a) shows the comparison between numerical and experimental temperatures at O.P. A and a strong agreement can be noticed between the two datasets (errors are always lower than 5% in magnitude). This is a further confirmation of the quality of the adopted 2D and 3D models. In particular, the reliable estimation of the temperatures means that magnitude and distribution of the losses are properly captured and the adopted combination of the Halpin-Tsai and ROM approaches to synthetize copper, air, enamel and epoxy material properties in radial, tangential and axial directions is a valuable strategy.

Since experimental data from the O.P. A are exploited not only for validation but also for ad-hoc calibration of the model, the actual validation of the numerical methodology is carried out against the experimental data of the operating conditions B and C. In this regard, it is important to highlight that, moving from the O.P. A to the O.Ps. B and C, no case-to-case tuning is carried out and the numerical setup is the same with the only exceptions which are, as obvious, heat sources coming from the 2D simulations and friction losses. The temperature variation between the inlet and outlet sections of the coolant predicted by the CFD model agrees with the experimental counterpart for both the conditions, as shown in Table 9. A strong agreement is noticed also in terms of pointwise

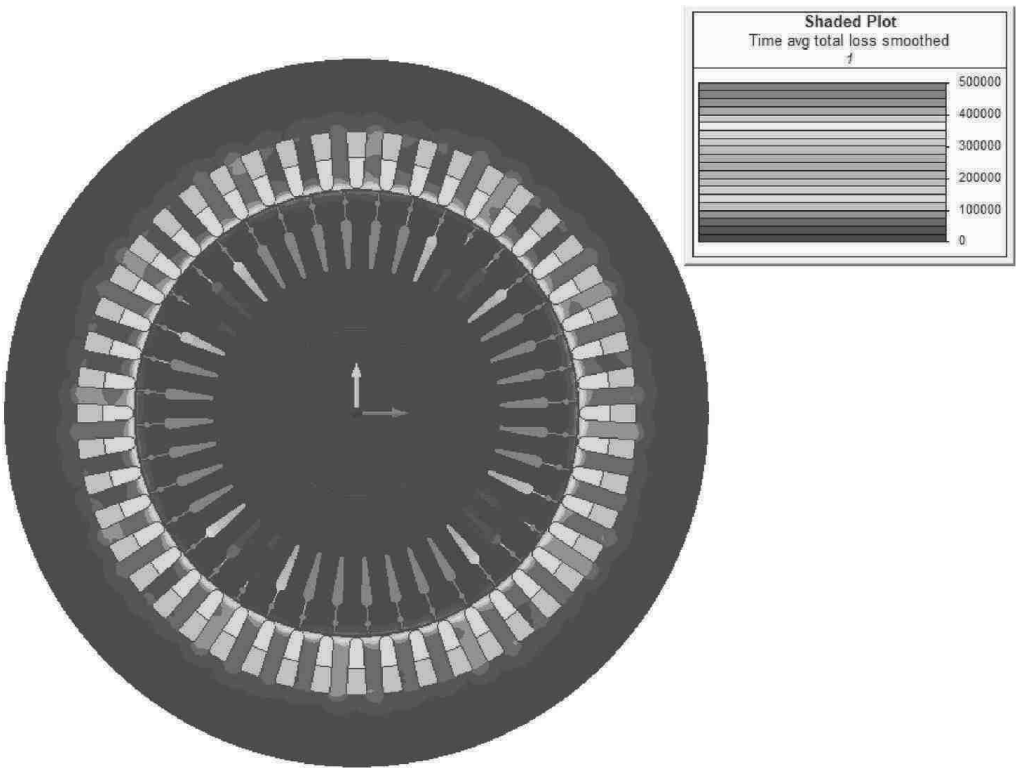

Fig. 11. –Time-average distribution of the total losses. Values are expressed in mW.

Table 9
Experimental and numerical temperature variations between inlet and outlet sections of the cooling jacket are reported for the different investigated conditions.

	Toutlet-Tinlet [°C]		
	O.P. A	O.P. B	O.P. C
Exp	6.3	4.5	7.4
CFD	6.2	4.4	7.5

temperature distribution, as shown in Figs. 12b) and 12c). The error is always lower than 5% in magnitude, as a demonstration of the predictive capabilities of the methodology. Figs. 13a), 13b) and 13c) show the temperature fields predicted by the CFD simulations on an axial plane at the investigated operating points. As expected, an axisymmetric temperature field is computed. Focusing on the outer region of the stator, in the axial direction, slightly higher temperatures are predicted in both solid and fluid domains moving towards the outlet section of the cooling jacket, for each operating point. This is due to the temperature increase of the water that decreases its capability to remove heat. The maximum temperatures are reached in the rotating bodies which are (partly) thermally insulated from the stator by air and bearings and they are the main responsible for the heat power generation. Therefore, rotor and shaft are the hardest bodies to cool. The rotor transfers heat mainly to the air by forced convection due to the rotating motion, while a smaller amount of heat moves through the shaft up to the case. Furthermore, a significant axial temperature gradient develops along rotor and shaft, due to their low axial conductivities. A hollow shaft cooled by a refrigerant fluid could be beneficial for handling high temperatures. The heat produced by the end windings mainly moves towards the stator slots where it adds to the heat produced by the active windings and, then, both head radially through the stator and finally to the motor housing.

6. Conclusions

In the present study, a numerical methodology for the thermal analysis of an electric motor is proposed. It is based on both 3D-CFD CHT and 2D-FE electromagnetic simulations and it is validated against experimental temperature measurements, at different operating conditions, on a three-phase induction motor.

In order to reduce the computational cost, a dedicated modelling of the coil in the stator slot is proposed, which is based on an equivalent homogeneous orthotropic material able to mimic the real component. Radial and tangential thermal conductivities of the copper coil are defined by Halpin-Tsai approach, while along the axial direction the Rule of Mixture is applied.

Particular care is dedicated to the modelling of the fluid domains as well, namely air in the motor case and refrigerant in the cooling jacket.

The main power losses adopted as heat source in the 3D-CFD model are provided by electromagnetic simulations which are able to properly estimate the motor output too. In particular, they provide both magnitude and distribution of the losses among the solid

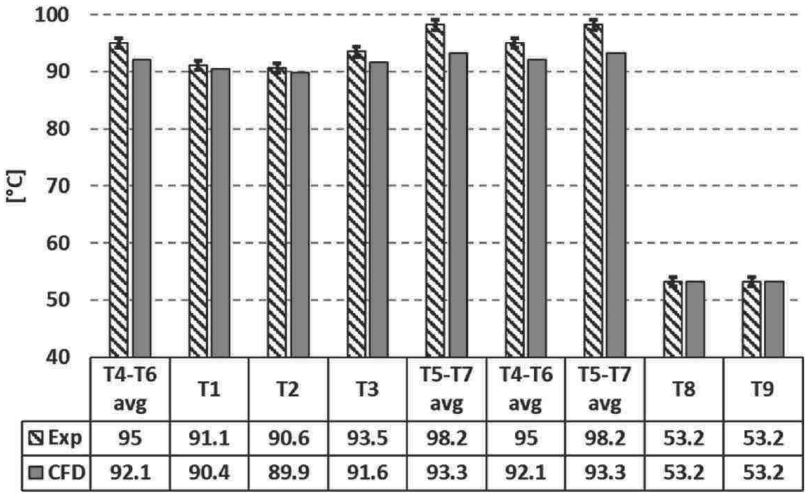

	T4-T6 avg	T1	T2	T3	T5-T7 avg	T4-T6 avg	T5-T7 avg	T8	T9
Exp	95	91.1	90.6	93.5	98.2	95	98.2	53.2	53.2
CFD	92.1	90.4	89.9	91.6	93.3	92.1	93.3	53.2	53.2

a)

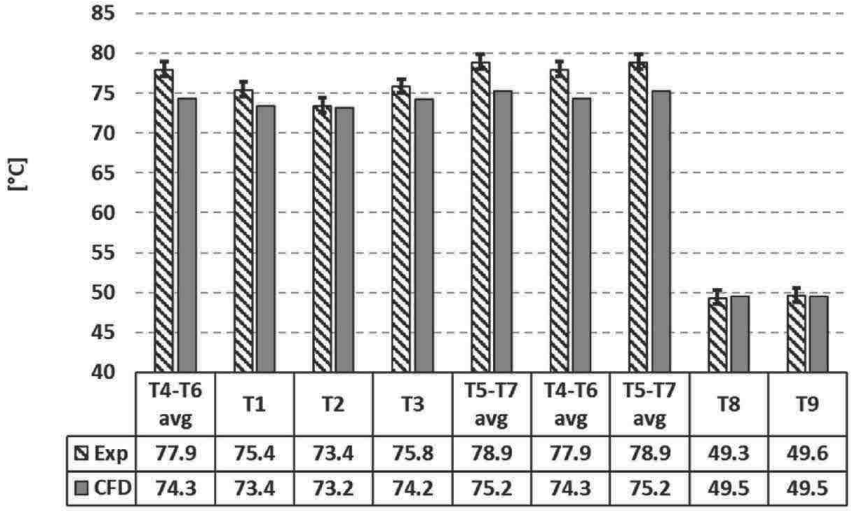

	T4-T6 avg	T1	T2	T3	T5-T7 avg	T4-T6 avg	T5-T7 avg	T8	T9
Exp	77.9	75.4	73.4	75.8	78.9	77.9	78.9	49.3	49.6
CFD	74.3	73.4	73.2	74.2	75.2	74.3	75.2	49.5	49.5

b)

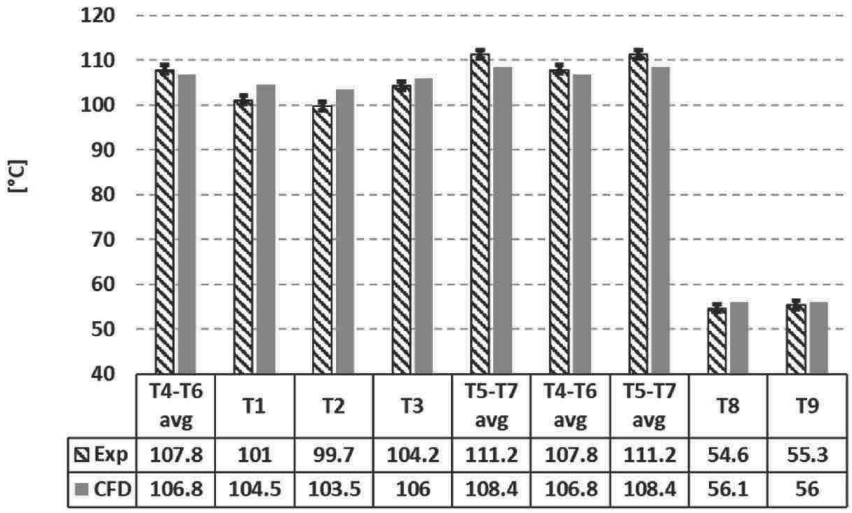

	T4-T6 avg	T1	T2	T3	T5-T7 avg	T4-T6 avg	T5-T7 avg	T8	T9
Exp	107.8	101	99.7	104.2	111.2	107.8	111.2	54.6	55.3
CFD	106.8	104.5	103.5	106	108.4	106.8	108.4	56.1	56

c)

(caption on next page)

Fig. 12. Local temperatures measured in the experiments and simulations (by thermocouples and numerical probes, respectively) are shown for O.P. A (a), O.P. B (b) and O.P. C (c).

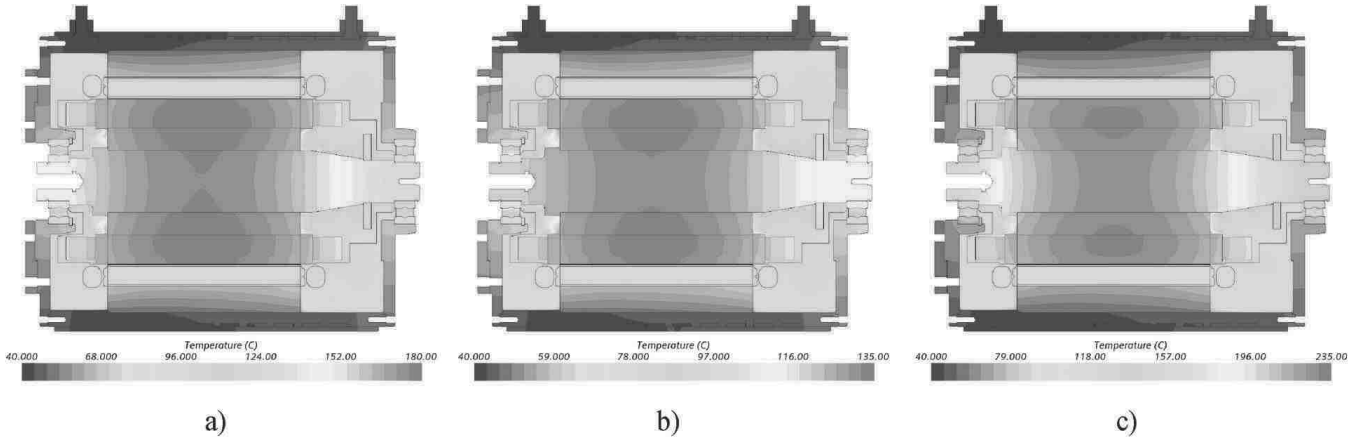

Fig. 13. Temperature fields of solid bodies and fluid domains are reported on an axial plane for O.P. A a), O.P. B b) and O.P. C c).

components. The 2D electromagnetic simulations are validated against experimental evidences in terms of performance and total losses of the motor.

Thanks to the detailed modelling of components, properties and losses, the thermal field of the engine is fairly reproduced, i.e. the error compared to the experimental measurements is at maximum 5%, for all the investigated conditions.

Finally, the temperature fields predicted by the 3D-CFD thermal model are presented and they allow to identify the rotor block as the most critical region of the motor.

CRediT authorship contribution statement

Clara Iacovano: Writing – original draft, Validation, Software, Methodology, Investigation, Formal analysis, Conceptualization. **Fabio Berni:** Writing – original draft, Validation, Software, Methodology, Investigation, Formal analysis, Conceptualization. **Giuseppe Cicalese:** Methodology, Investigation, Conceptualization. **Stefano Nuzzo:** Writing – original draft, Validation, Software, Investigation, Formal analysis, Conceptualization. **Stefano Fontanesi:** Writing – original draft, Supervision, Conceptualization.

Declaration of competing interest

The authors declare that they have no known competing financial interests or personal relationships that could have appeared to influence the work reported in this paper.

Data availability

The authors do not have permission to share data.

Acknowledgment

The authors wish to thank Lucchi R. s.r.l. for providing the geometry of the motor, the experimental data and a very kind support during the activity.

Moreover, the authors gratefully acknowledge the University of Modena and Reggio Emilia for supporting the activity by the “Fondo di Ateneo per la Ricerca 2023 per il finanziamento di piani di sviluppo dipartimentale nell’ambito della ricerca” (FARD-2023).

APPENDIX A

A sensitivity is proposed in the present appendix, in order to demonstrate that the adopted numerical mesh is sufficiently fine to ensure grid-independent results. Beside the mesh utilized for the simulations presented in the main text of the paper and characterized by nearly 20 million cells, a refined one is tested (roughly targeting half of the cell size adopted for the presented analyses). The refined mesh is made of nearly 80 million cells. The comparison between the grids is reported in Fig. 14. For brevity, only O.P. A is considered for the sensitivity. Despite the huge increase of computational time (nearly 4 times the one related to the coarse grid), the variations of the resulting temperatures are lower than 0.3%. This is an evidence that the adopted coarse grid is able to provide grid independent results.

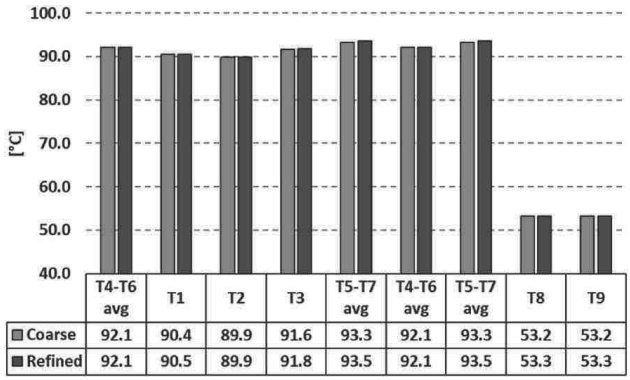

	T4-T6 avg	T1	T2	T3	T5-T7 avg	T4-T6 avg	T5-T7 avg	T8	T9
Coarse	92.1	90.4	89.9	91.6	93.3	92.1	93.3	53.2	53.2
Refined	92.1	90.5	89.9	91.8	93.5	92.1	93.5	53.3	53.3

Fig. 14. Comparison in terms of temperature between coarse and fine grids is shown for O.P. A.

References

[1] Jer-Huan Jang, Han-Chieh Chiu, Wei-Mon Yan, M.C. Tsai, Pin-Yuan Wang, "Numerical study on electromagnetics and thermal cooling of a switched reluctance motor", Case Stud. Therm. Eng., https://doi.org/10.1016/j.csite.2015.05.001.

[2] M.H. Park, S.C. Kim, Thermal characteristics and effects of oil spray cooling on in-wheel motors in electric vehicles, Appl. Therm. Eng. 152 (2019) 582–593. S.

[3] Nuzzo, D. Barater, C. Gerada and P. Vai, "Hairpin windings: an Opportunity for next-generation E-motors in transportation," in IEEE Industrial Electronics Magazine, doi: 10.1109/MIE.2021.3106571.

[4] E. Gundabattini, R. Kuppan, D. G. Solomon, A. Kalam, D.P. Kothari, R. A. Bakar, "A review on methods of finding losses and cooling methods to increase efficiency of electric machines", Ain Shams Eng. J., https://doi.org/10.1016/j.asej.2020.08.014.

[5] Kea-Ho Lee, Hyun-Rok Cha, Young-Bae Kim, Development of an interior permanent magnet motor through rotor cooling for electric vehicles, Appl. Therm. Eng. (2016), 10.1016/j.applthermaleng.2015.11.022.

[6] F. Qi, I. Ralev, A. Stippich, R.W. De Doncker, Model predictive overload control of an automotive switched reluctance motor for frequent rapid accelerations, in: 2016 19th International Conference on Electrical Machines and Systems (ICEMS), 2016, pp. 1–6.

[7] A. La Rocca, A. Fregni, S. La Rocca, C. Gerada, Numerical thermal modelling of multiphase spray cooling of hairpin windings, in: International Conference on Electrotechnical Complexes and Systems (ICOECS), 2020, https://doi.org/10.1109/ICOECS50468.2020.9278458.

[8] D. Staton, A. Boglietti, A. Cavagnino, Solving the more difficult aspects of electric motor thermal analysis, in: IEEE International Electric Machines and Drives Conference, 2003, https://doi.org/10.1109/IEMDC.2003.1210320.

[9] P.S. Ghahfarokhi, A. Podgornovs, A.J. Marques Cardoso, A. Kallaste, A. Belahcen, T. Vaimann, Thermal modeling of a TEFC synchronous reluctance motor, in: 2021 IEEE 62nd International Scientific Conference on Power and Electrical Engineering of Riga, Technical University (RTUCON), 2021, https://doi.org/10.1109/RTUCON53541.2021.9711740.

[10] S. Touhami, Y. Bertin, Y. Lefèvre, J. Llibre, C. Hénaux, et al., Lumped parameter thermal model of permanent magnet synchronous machines", Jul 2017, Toulouse, France, Electrimacs (2017) 1–6. hal-01649396.

[11] Y. Xia, Y. Han, Y. Xu and M. Ai, "Analyzing temperature rise and fluid flow of high-power-density and high-voltage induction motor in the starting process," in IEEE Access, doi: 10.1109/ACCESS.2019.2899346.

[12] S.T. Lundmark, A. Acquaviva, A. Bergqvist, Coupled 3-D thermal and electromagnetic modelling of a liquid-cooled transverse flux traction motor, in: 2018 XIII International Conference on Electrical Machines (ICEM), 2018, https://doi.org/10.1109/ICELMACH.2018.8506835.

[13] P. Ponomarev, M. Polikarpova, J. Pyrhönen, Thermal modeling of directly-oil-cooled permanent magnet synchronous machine, in: 2012 XXth International Conference on Electrical Machines, 2012, https://doi.org/10.1109/ICElMach.2012.6350138.

[14] A. Corsini, F. Rispoli, A.G. Sheard, et al., Computational analysis of noise reduction devices in axial fans with stabilized finite element formulations, Comput. Mech. 50 (2012) 695–705, https://doi.org/10.1007/s00466-012-0789-4.

[15] S.R. Krishna, A.R. Krishna, K. Ramji, Reduction of motor fan noise using CFD and CAA simulations, Appl. Acoust. 72 (2011) 982–992, https://doi.org/10.1016/j.apacoust.2011.06.008.

[16] L. Chunxi, W.S. Ling, J. Yakui, The performance of a centrifugal fan with enlarged impeller, Energy Convers. Manag. 52 (2011) 2902–2910, https://doi.org/10.1016/j.enconman.2011.02.026.

[17] E. Galloni, P. Parisi, F. Marignetti, G. Volpe, "CFD analyses of a radial fan for electric motor cooling", Therm. Sci. Eng. Prog., https://doi.org/10.1016/j.tsep.2018.10.003.

[18] Hongmin Li, "Cooling of a permanent magnet electric motor with a centrifugal impeller", Int. J. Heat Mass Tran., https://doi.org/10.1016/j.ijheatmasstransfer.2009.09.022.

[19] T. Hong, M. Rakotovao, M. Henner, S. Moreau, et al., Thermal analysis of electric motors in engine cooling fan systems, SAE Technical Paper 2001-01-1017 (2001), https://doi.org/10.4271/2001-01-1017.

[20] A. Deriszadeh, F. de Monte, M. Villani, L. Di Leonardo, Hydrothermal performance of ethylene glycol and water mixture in a spiral channel for electric motor cooling, in: 21st European Conference on Power Electronics and Applications (EPE '19 ECCE Europe), 2019, https://doi.org/10.23919/EPE.2019.8914967.

[21] Marco Satrústegui, Miguel Martinez-Iturralde, Juan C. Ramos, Patxi Gonzalez, Gorka Astarbe, Ibon Elosegui,"Design criteria for water cooled systems of induction machines", Appl. Therm. Eng., https://doi.org/10.1016/j.applthermaleng.2016.12.031.

[22] Ali Deriszadeh, Filippo de Monte, On the Thermofluid Characteristics of a Nanofluid for Electric Motor Cooling, ICCHMT, Rome, Italy, 2019, pp. 3–6. September 2019.

[23] A. Tikadar, D. Johnston, N. Kumar, Y. Joshi, S. Kumar, "Comparison of electro-thermal performance of advanced cooling techniques for electric vehicle motors", Appl. Therm. Eng., https://doi.org/10.1016/j.applthermaleng.2020.116182.

[24] A. Deriszadeh, F. de Monte, M. Villani, "Numerical thermal performance investigation of an electric motor passive cooling system employing phase, Change Materials (2021) doi=10.1115/HT2021-63506.

[25] Yalong Sun, Shiwei Zhang, Wei Yuan, Yong Tang, Jingrong Li, Kairui Tang, "Applicability study of the potting material based thermal management strategy for permanent magnet synchronous motors", Appl. Therm. Eng., https://doi.org/10.1016/j.applthermaleng.2018.12.141.

[26] A. La Rocca, A. Fregni, S. La Rocca, C. Gerada, Numerical thermal modelling of multiphase spray cooling of hairpin windings, in: International Conference on Electrotechnical Complexes and Systems (ICOECS), 2020, https://doi.org/10.1109/ICOECS50468.2020.9278458.

[27] F. Guo, C. Zhang, Oil-cooling method of the permanent magnet synchronous motor for electric vehicle, Energies 12 (2019) 2984, https://doi.org/10.3390/en12152984.

[28] J. Zeng, X. Sun, Z. Qian, Thermal simulation of an oil-cooled permanent magnet synchronous motor, in: 2017 IEEE International Electric Machines and Drives Conference (IEMDC), 2017, https://doi.org/10.1109/IEMDC.2017.8001872.
[29] F. Zhang et al., "A thermal modeling approach and experimental validation for an oil spray-cooled hairpin winding machine," in IEEE Transactions on Transportation Electrification, doi: 10.1109/TTE.2021.3067601.
[30] Tanguy Davin and Julien Pellé and Souad Harmand and Robert Yu, "Experimental study of oil cooling systems for electric motors", Appl. Therm. Eng., https://doi.org/10.1016/j.applthermaleng.2014.10.060.
[31] C. Liu, et al., Experimental investigation on oil spray cooling with hairpin windings, in: IEEE Transactions on Industrial Electronics, Sept, 2020, https://doi.org/10.1109/TIE.2019.2942563.
[32] C. Srinivasan, X. Yang, J. Schlautman, D. Wang, et al., Conjugate heat transfer CFD analysis of an oil cooled automotive electrical motor, SAE Technical Paper 2020-01-0168 (2020), https://doi.org/10.4271/2020-01-0168.
[33] J. Montonen, J. Nerg, M. Polikarpova, J. Pyrhönen, Integration principles and thermal analysis of an oil-cooled and - lubricated permanent magnet motor planetary gearbox drive system, in: IEEE Access, 2019, https://doi.org/10.1109/ACCESS.2019.2919506.
[34] Yalong Sun, Shiwei Zhang, Gong Chen, Yong Tang, Fuye Liang, "Experimental and numerical investigation on a novel heat pipe based cooling strategy for permanent magnet synchronous motors", Appl. Therm. Eng., https://doi.org/10.1016/j.applthermaleng.2020.114970.
[35] Guoyun Fang and Wei Yuan and Zhiguo Yan and Yalong Sun and Yong Tang, "Thermal management integrated with three-dimensional heat pipes for air-cooled permanent magnet synchronous motor", Appl. Therm. Eng., doi=https://doi.org/10.1016/j.applthermaleng.2019.02.120.
[36] J. Huang et al., "A hybrid electric vehicle motor cooling system design, model, and control," in IEEE Transactions on Vehicular Technology, doi: 10.1109/TVT.2019.2902135.
[37] H. Fujita, A. Itoh, T. Urano, Newly developed motor cooling method using refrigerant, World Electr. Veh. J. (2019), https://doi.org/10.3390/wevj10020038.
[38] Yongsheng Li, Congbo Li, Akhil Garg, Liang Gao, Wei Li, Heat dissipation analysis and multi-objective optimization of a permanent magnet synchronous motor using surrogate assisted method, Case Stud. Therm. Eng. 27 (2021), https://doi.org/10.1016/j.csite.2021.101203.
[39] D.G. Solomon, A. Greco, C. Masselli, E. Gundabattini, R.S. Rassiah, R. Kuppan, A review on methods to reduce weight and to increase efficiency of electric motors using lightweight materials, novel manufacturing processes, magnetic materials and cooling methods, in: Annales de Chimie - Science des Matériaux, 2020, https://doi.org/10.18280/acsm.440101.
[40] P.S. Ghahfarokhi, A. Podgornovs, A.J.M. Cardoso, A. Kallaste, A. Belahcen, T. Vaimann, AC losses analysis approaches for electric vehicle motors with hairpin winding configuration, in: IECON 2021 – 47th Annual Conference of the IEEE Industrial Electronics Society, 2021, https://doi.org/10.1109/IECON48115.2021.9589339.
[41] P.S. Ghahfarokhi, A. Podgornovs, A.J. Marques Cardoso, A. Kallaste, A. Belahcen, T. Vaimann, Hairpin windings manufacturing, design, and AC losses analysis approaches for electric vehicle motors, in: 2021 11th International Electric Drives Production Conference (EDPC), 2021, https://doi.org/10.1109/EDPC53547.2021.9684208.
[42] G. Venturini, G. Volpe, M. Villani, M. Popescu, Investigation of cooling solutions for hairpin winding in traction application, in: 2020 International Conference on Electrical Machines (ICEM), 2020, https://doi.org/10.1109/ICEM49940.2020.9271026.
[43] A. Selema, M.N. Ibrahim, P. Sergeant, Mitigation of high-frequency eddy current losses in hairpin winding machines, Machines (2022), https://doi.org/10.3390/machines10050328.
[44] A. Reinap, M. Andersson, F.J. Márquez-Fernández, P. Abrahamsson, M. Alaküla, Performance estimation of a traction machine with direct cooled hairpin winding, in: 2019 IEEE Transportation Electrification Conference and Expo (ITEC), 2019, https://doi.org/10.1109/ITEC.2019.8790545.
[45] Ogawa Jun, Fukui Satoshi, Oka Tetsuo, Sato Takao, Fushimi Atsumu, Shoda Takuya, Influence of the arrangement of HTS tapes inserted in an iron core on AC loss characteristics, IEEE Trans Appl Conduct 24 (3) (2014) 6600204.
[46] S. Nuzzo, P. Bolognesi, G. Decuzzi, P. Giangrande, M. Galea, A consequent-Pole hybrid exciter for synchronous generators, IEEE Trans. Energy Convers. 36 (1) (March 2021) 368–379, https://doi.org/10.1109/TEC.2020.3012198.
[47] L. Idoughi, X. Mininger, F. Bouillault, L. Bernard, E. Hoang, Thermal model with winding homogenization and FIT discretization for stator slot, IEEE Trans. Magn. 47 (12) (Dec. 2011) 4822–4826, https://doi.org/10.1109/TMAG.2011.2159013.